

LINEAR MODE HgCdTe AVALANCHE PHOTODIODES FOR PHOTON COUNTING APPLICATIONS*

William Sullivan III¹, Jeffrey Beck, Richard Scritchfield, Mark Skokan, and Pradip Mitra

DRS Technologies, C4ISR Group, 13544 N. Central Expressway, Dallas, Texas, 75243

Xiaoli Sun and James Abshire

NASA Goddard Space Flight Center, Greenbelt, Maryland 20771

Darren Carpenter and Barry Lane

A/DIC Inc., 740 Florida Central Parkway, Longwood, FL 32750

Abstract

An overview of recent improvements in the understanding and maturity of linear mode photon counting with HgCdTe electron-initiated avalanche photodiodes is presented. The first HgCdTe LMPC 2x8 format array fabricated in 2011 with 64 μm pitch was a remarkable success in terms of demonstrating a high single photon signal to noise ratio of 13.7 with an excess noise factor of 1.3-1.4, a 7 ns minimum time between events, and a broad spectral response extending from 0.4 μm to 4.2 μm . The main limitations were a greater than 10x higher false event rate than expected of > 1 MHz, a 5-7x lower than expected APD gain, and a photon detection efficiency of only 50% when greater than 60% was expected. This paper discusses the reasons behind these limitations and the implementation of their mitigations with new results.

¹ Corresponding author information: William Sullivan III: billy.sullivan@drs.com, 214-996-2861

*Supported by a NASA Earth Science Technology Office Advanced Component Technology program

I. Introduction

Mid-wave infrared (MWIR) HgCdTe electron-initiated avalanche photodiodes (e-APDs) with single photon sensitivity have many applications including photon counting, ladar/lidar, quantum cryptography, and free space optical communication links. Photodiode receivers with single photon sensitivity offer significant device and system level benefits such as enabling a reduction of the optical source's size, weight, and power requirements as fewer received photons are required for detection. APDs are operated in two different modes: Geiger mode and linear mode. Geiger mode APDs are biased above their breakdown voltage and the breakdown process is initiated upon absorbing a single photon resulting in an avalanche gain in the millions. As such, they require a quenching circuit to stop the breakdown process and reset the circuit. This quenching action requires a finite amount of time (typically longer than 1 μ s), and leaves the detector blind to another incoming photon for that amount of time. Compared to Geiger mode APDs, linear mode APDs are biased below the breakdown voltage. As breakdown doesn't occur, there is no dead-time and quenching circuits are not required. Gains are typically on the order of 10-10,000. The minimum time between photon events is limited by the combined bandwidth of the APD and the pre-amplifier, and Beck *et al.* have shown it to be less than 10 ns [1,2] which was pre-amplifier bandwidth limited. DRS previously reported on cylindrical geometry linear mode e-APDs in a 2x8 format array with photon counting sensitivity that showed robust photon counting performance, although three main unexpected limitations were discovered and are listed in Table 1 [1,2]. Under a NASA Earth Science Technology Office Advanced Component Technology program these three limitations were investigated and addressed, and the improvements that were implemented are discussed in this paper. The first limitation was that the false event rate² (FER) at 50% photon detection efficiency (PDE) was over 1 MHz. The large discrepancy between the test diode FER measurements of 30 kHz and the array FER measurement of >1 MHz was concluded to be from readout integrated circuit (ROIC) glow emitted photons being absorbed by the APDs which artificially increased the FER. This was corrected for in the current 2014 lot by depositing a metal blocking layer on top of the ROIC to shield the detectors from the glow photons. The next limitation was that the

² The term "False Event Rate" is used as a cumulative term that lumps all threshold exceedance events caused by ROIC noise and detector "dark" current. The detector induced events are those due to intrinsic detector dark current, current due to photons emitted by the ROIC, stray photons in the Dewar, and thermal background flux through the cold filter.

maximum APD gain was only 470 at 13 V bias, when a gain of over 1000 was expected. This was due to larger than expected junction diameters, and was corrected for by reducing the junction diameter in the current lot. The final limitation was the maximum PDE was only 50%, when a PDE of greater than 60% was expected. This was due to the lower than expected gain as well as limited data processing capabilities, and was corrected for by increasing the diodes' gain as well as using enhanced data processing algorithms.

Table 1: Overview of Limitations Discovered in 2011 LMPC Array

Limitation to be Addressed	2011 LMPC Array	Two 2014 Arrays	
		A8327-8-2	A8327-14-1
1.) False Event Rate at 50% PDE	> 1 MHz	151 kHz	158 kHz
2.) Maximum APD Gain	470	1910	1100
3.) Maximum Photon Detection Efficiency	50%	72%	66%

II. Avalanche Photodiode Design

The 2014 arrays were fabricated in a similar fashion as described by Beck *et al.* on the 2011 arrays [1]. Briefly, the APDs were fabricated from $\text{Hg}_{1-x}\text{Cd}_x\text{Te}$ grown using liquid phase epitaxy (LPE) with $x = 0.33$ for a cutoff of $4.3 \mu\text{m}$ at 77 K. The arrays used DRS' High Density Vertically Integrated Photodiode (HDVIP™) architecture: a front face illuminated p-around-n cylindrical homo-junction diode structure that features low capacitance for high bandwidth, low dark current defects due to the vertical orientation of the p-n junction which results in a low cross section for intersecting dislocations emanating from the LPE growth interface, and interdiffused CdTe surface passivation on both array surfaces for low dark current. The arrays were fabricated on the same ROICs as were used on the 2011 LMPC arrays. Briefly, the custom Si ROIC features an analog output and a digital comparator output with individually settable thresholds for each pixel, although the digital outputs were not used in the present testing. The unit cell features an adjustable gain resistive transimpedance amplifier (RTIA) with a designed bandwidth of 175 MHz and a designed single photon signal-to-noise ratio (SNR) of 23.2 at an APD gain of 1000. A partial single channel schematic is shown in Fig. 1 highlighting the analog signal path. During the NASA ACT program, long after the ROICs had been fabricated, a parasitic analysis performed on the ROIC using Silvaco® Hipex determined that unaccounted for stray capacitances in the unit cell's design limited the bandwidth and the full 175 MHz wasn't

achieved. Simulations and measurements show that the bandwidth was only approximately 71 MHz and the single photon SNR was only 13.9, which agrees well with measured values shown in Sec. IV.e and is discussed in more detail there.

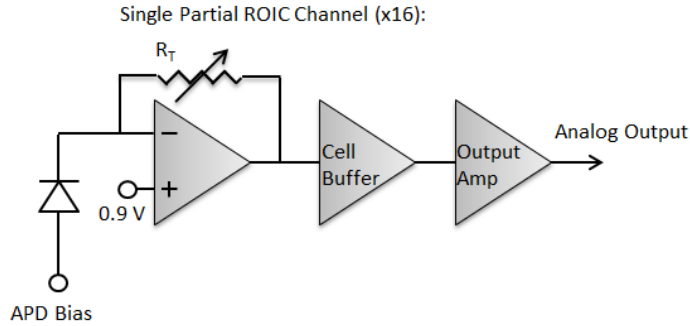


Figure 1: Partial single channel ROIC architecture.

III. Experimental Setup

The arrays were operated in a custom LN₂ pour-fill lab Dewar at 82 K that featured extensive stray light shielding. This was implemented in an effort to reduce the FER and ensure the high FER measured in 2011 wasn't due to stray thermal background flux. Two cold filters, each with a pass band of 1.2-1.8 μm and >OD4 blocking from 2-5 μm , were stacked to provide >OD8 blocking out of band with a combined 75% in-band transmission at 1550 nm. Using a $f/1.5$ cold aperture, the calculated combined in-band and out-of-band background count rate was 12.2 kHz. When performing optical tests with the laser, the system was calibrated so that the flux used was what was incident upon the detector surface (i.e. the cold filters' and window's transmissions were calibrated out). Two different fiber-coupled lasers were used for characterization, a 1 ns pulsed laser and a cw laser. Both were 1550 nm. The lasers were focused using either a 0.26 or 0.42 NA objective lens that was mounted to a stepper-motor controlled XYZ stage with sub-micron movement capability. This system was used to move the focused laser to the area of interest in the pixel, typically in the center p-type HgCdTe region between the four junctions as shown in Fig. 2.

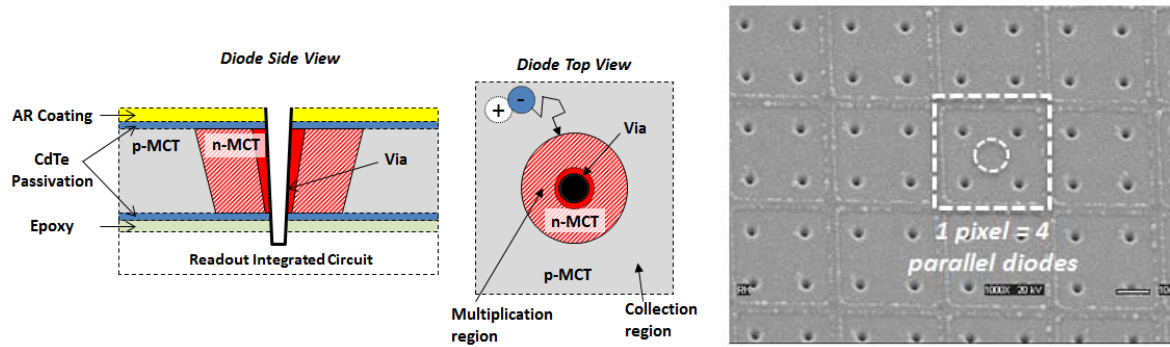


Figure 2: Left: DRS' HDVIP™ diode geometry. Right: SEM array image with pixel outline shown. One pixel is composed of 4 parallel diodes. The dashed circle shows the typical focused laser illumination location.

IV. Results

Five arrays were evaluated from lot A8327, each with different processing splits. The splits enable characterizing the effects of a certain processing step while keeping all of the other processing steps the same. Four of the five arrays were Hg vacancy (V_{Hg}) doped with N_A of $\sim 1 \cdot 10^{16} \text{ cm}^{-3}$ and one was Cu+ V_{Hg} doped with N_A of $\sim 2 \cdot 10^{16} \text{ cm}^{-3}$. Four arrays had a single layer ZnS anti-reflection (AR) coating of 92% efficiency, while one array had a double layer ZnS+SiO₂ AR coating of >98% efficiency. Finally, three arrays had a ROIC glow blocking metal layer deposited while two did not. All of the arrays received the same processing steps except for these splits. Table 3 summarizes the performance of five of the arrays, and Fig. 3 shows the 16-pixel-mean PDE vs. FER for each array under a cw flux of $5 \cdot 10^6$ photons/s.

Table 2: Array Processing Splits

Array	P-type Doping	ROIC Glow Mirror Blocking Metal Layer	AR Coating
A8327-2-2	V_{Hg}	Yes	ZnS
A8327-8-2	Cu + V_{Hg}	Yes	ZnS
A8327-14-1	V_{Hg}	Yes	ZnS
A8327-14-2	V_{Hg}	No	ZnS
A8327-20-2	V_{Hg}	No	ZnS + SiO ₂

The three arrays with the mirror blocking metal exhibited a 5x decrease in FER compared to the two without it confirming that ROIC glow was indeed contributing to the inflated FER. A8327-8-2 had a slightly higher PDE due to its expected longer electron diffusion length and higher gain compared to the other two V_{Hg} -only doped samples with the mirror blocking metal layer. A8327-20-2 had a higher PDE than A8327-14-2 due to the more efficient AR coating. Overall, the higher PDEs shown in Fig. 3 are close to theoretical predictions and simulations.

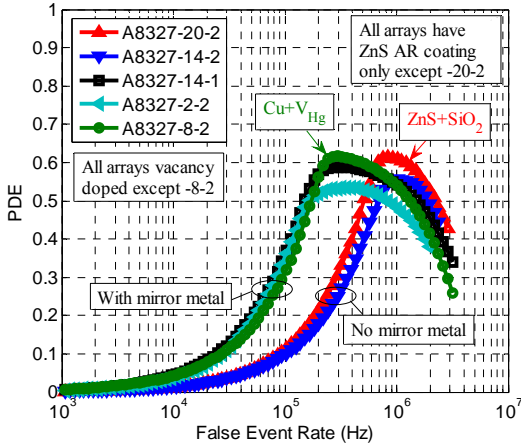


Figure 3: 16 pixel mean PDE vs FER for 5 different 2x8 arrays at an APD bias of 12.9 V and under cw flux of $5 \cdot 10^6$ photons/s. The 3 arrays with the mirror blocking metal exhibited a 5x decrease in FER compared to the 2 arrays without it.

Table 3: 2011 and 2014 Array Performance Summary.

	2011 LMPC Array	Two 2014 Arrays	
		A8327-8-2	A8327-14-1
Maximum PDE (focused spot)	50% (at 14 V APD bias)	72% (at 12.9 V)	66% (at 12.9 V)
APD Gain	470 (at 13 V)	1910 (at 12.9 V)	1100 (at 12.9 V)
FER at 50% PDE	> 1 MHz	151 kHz	158 kHz
Mean Single Photon SNR	13.7	21.9	12.3
Excess Noise Factor	1.3-1.4	1.25	1.20
Measured RMS Jitter (ps)	632 ps	2370 ps	1570 ps
Minimum Time Between Events (ns)	8 ns	Not measured	9 ns

a. False Event Rate

It has been shown that Si CMOS transistors in saturation emit photons due to hot carrier effects and the emission rate is up to 10^4 higher at 80 K compared to 300 K [3]. In the vertically integrated structure that DRS uses, and without any metal blocking layers, these ROIC generated glow photons are in the “direct line of sight” of the array and have energies within the detectors’ spectral response. Also, uncovered high power buffers that were present around the perimeter of the ROIC (to drive the signals off-chip) were very likely emitting photons as well. To validate that ROIC glow was indeed the major source of the FER increase, two sister arrays were fabricated in the 2014 lot from the same HgCdTe bar: one without a metal mirror blocking layer (A8327-14-2) to simulate the 2011 array, and one with a 96.9% coverage single metal blocking layer (A8327-14-1) deposited on top of the ROIC before the HgCdTe was mounted. The properties of the HgCdTe across the bar are typically very uniform allowing for a comparison of only the effect of the metal layer and not the HgCdTe dark count rate. Figure 4 shows a 16-pixel mean PDE vs. FER comparison of A8327-14-1 and A8327-14-2. Each pixel’s FER is ≤ 200 kHz on A8327-14-1, with an average FER of 158 kHz, at the optimum threshold of 4.8 mV yielding $\text{PDE} \geq 50\%$ across all pixels as shown in Fig. 4. Alternatively, the 16-pixel average FER of A8327-14-2 was 4.8x higher at 767 kHz. Optimization of the ROIC biases reduced A8327-14-1’s FER by another factor of 2 yielding almost an order of magnitude decrease in FER compared to the 2011 results.

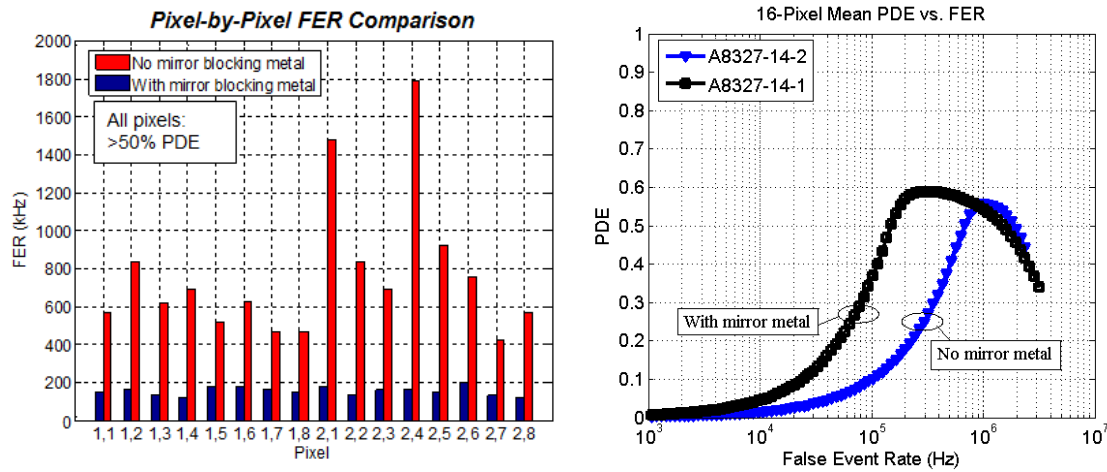


Figure 4: Left: FER vs. pixel at the optimum threshold of 4.8 mV. Right: 16-pixel mean PDE vs. FER showing $\geq 50\%$ PDE across all pixels on both arrays at a FER of < 200 kHz.

Although the FER was reduced, it still wasn't reduced down to measured test diode levels of 20 kHz or less, as shown in Fig. 5. This is likely due to the metal layer being only a semi-continuous single layer and the perimeter buffers were not covered by the mirror blocking metal as well. To reduce the FER down to the measured diode dark current rate of <20 kHz shown in Fig. 5, the ROIC needs to include multiple metal layers for 100% coverage directly under the detectors as well as blocking of the perimeter buffers.

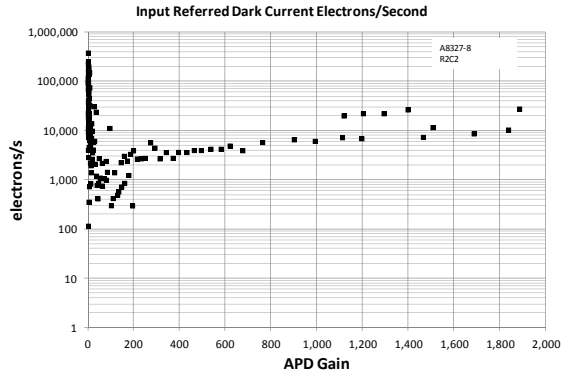


Figure 5: Gain normalized dark current of test diodes showing a maximum effective dark count rate of less than 30 kHz at gains up to 1900 [2].

b. Effect of Gain on PDE

The difference in p-type doping is shown in Fig. 6. A8327-8-2 shows a 5% higher PDE which could be due to its longer expected diffusion length, or more likely due to its higher gain.

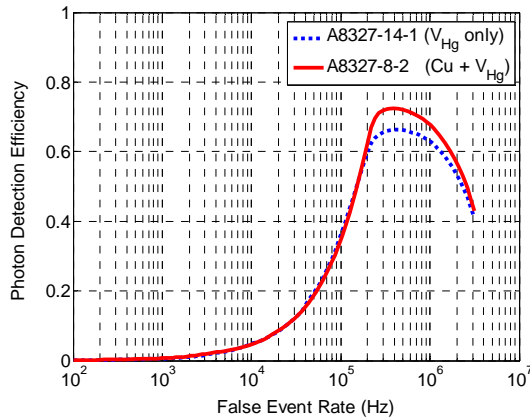


Figure 6: PDE vs. FER comparing the p-type doping.

c. APD Junction Diameter and Multiplication Region Width

The APD's junction diameter is a critical parameter in determining the performance of the detector. For a given APD pitch (in the 2x2 APD pixel configuration) the junction diameter determines the diffusion jitter and the electron collection efficiency (eCE), where the eCE is defined as the percentage of photoelectrons collected by the junctions. The APD gain is determined by the multiplication region width [4,5] which, in the case of the HDVIP structure, is determined by the junction and via diameters of the APD (c.f. Fig. 2). The excess noise factor also depends on the multiplication region width [5].

The PDE depends directly on the net photon to collected electron conversion efficiency. The conversion efficiency (CE) is the product of the quantum efficiency (QE), the fill factor, and the eCE. The spatial dependence of the electron collection efficiency is revealed by performing response spot scans over the area of the pixel. High resolution, 1- μm -step, surface spot scans were performed on an operating pixel to measure the PDE vs. location in the pixel and also to determine the junction diameter. The 1550 nm cw laser was focused using a 0.42 NA long working distance objective lens to a spot size of approximately 7 μm FWHM diameter and scanned across the pixel. Figure 7 shows the PDE vs. position spot scan of A8327-8-2. Figure 8 shows a PDE vs. position spot scan comparison of A8327-14-1 and A8327-8-2, and Fig. 9 compares the V_{Hg} doped sample with the 2011 array. Table 4 summarizes the junction diameter results.

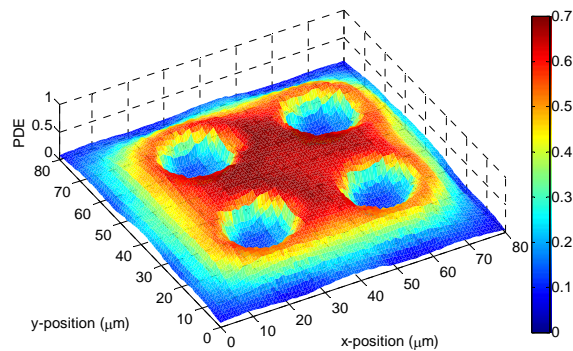


Figure 7: PDE vs. position inside a pixel of A8327-8-2. The central p-type area shows the highest PDE. The PDE falls off inside the junctions because the gain falls off rapidly, and finally the lowest PDE is inside the metal vias.

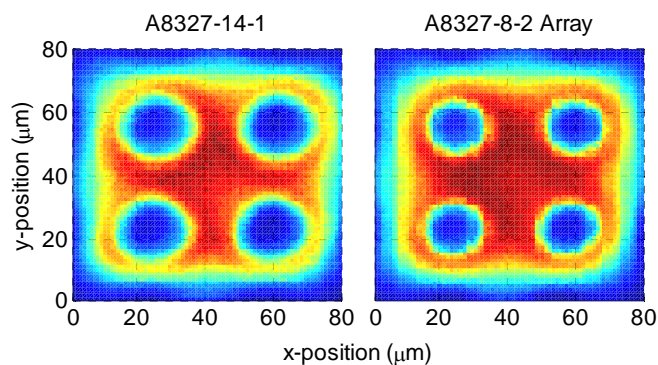


Figure 8: Surface spot scan of PDE vs. location of a single pixel. Left: Single pixel in A8327-14-1. Right: Single pixel in A8327-8-2.

The Cu+V_{Hg} doped sample, A8327-8-2, shows smaller junction diameters of approximately 22 μm while the V_{Hg} doped only sample, A8327-14-1, shows larger junction diameters of approximately 25 μm. This is expected as Cu+V_{Hg} doped samples have smaller junctions than V_{Hg}-doped-only samples do when etched in the same conditions, and all arrays had the same etch performed. Comparing the spot scan data to the 2011 array, its junctions are even larger at approximately 31 μm. Assuming a n⁺ diameter of 12 μm, A8327-8-2's junction width is approximately 5 μm, A8327-14-1's is 6.5 μm, and the 2011 array's is 9.5 μm. Larger diameter junctions result in lower gain at the same APD bias voltage and, for the same diode pitch, lower jitter, and this is observed in the 2011 array. Larger junctions should also have a higher eCE (effectively maximum PDE) assuming the same diode pitch and electron diffusion length; however, the 2011 array did not show a higher PDE than the current arrays with smaller junctions. This is likely due to its lower gain, as well as a more refined PDE vs. FER algorithm that is currently being used. It may also be partially due to the slightly lower excess noise factors in the current arrays.

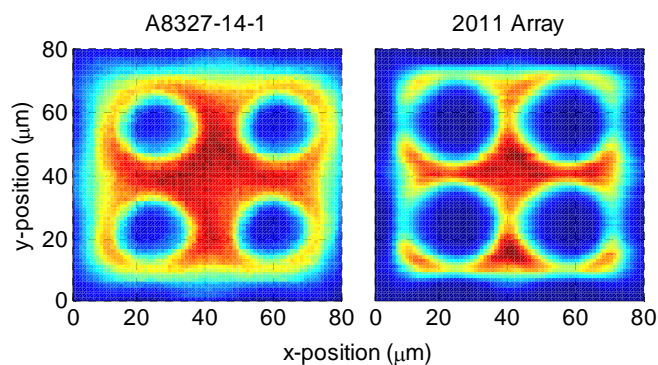


Figure 9: Surface spot scan of PDE vs. location of a single pixel. Left: Single pixel in A8327-14-1. Right: Single pixel in 2011 array.

Table 4: Summary of junction diameter, APD gain, rms jitter, maximum PDE, and excess noise factor for the three arrays.

Array	Junction Diameter	APD Gain	RMS Jitter	Maximum PDE	Excess Noise Factor
2011 Array	31 μm	470 (@ 13 V)	632 ps	0.5 (at 14 V APD bias)	1.30-1.40
A8327-14-1	25 μm	1100 (@ 12.9 V)	1570 ps	0.66 (at 12.9 V APD bias)	1.20
A8327-8-2	22 μm	1910 (@ 12.9 V)	2370 ps	0.72 (at 12.9 V APD bias)	1.25

i. Gain

Increased APD gains of up 1910 were measured on the operating arrays using 1550 nm light focused in the middle of the four junctions as shown in Fig. 10. The smaller measured junction width on A8327-8-2 agrees with the higher gain measured at the same bias voltage of 12.9 V. Gain across the four V_{Hg} doped only arrays was uniform with a mean gain of 1073 +/- 12%.

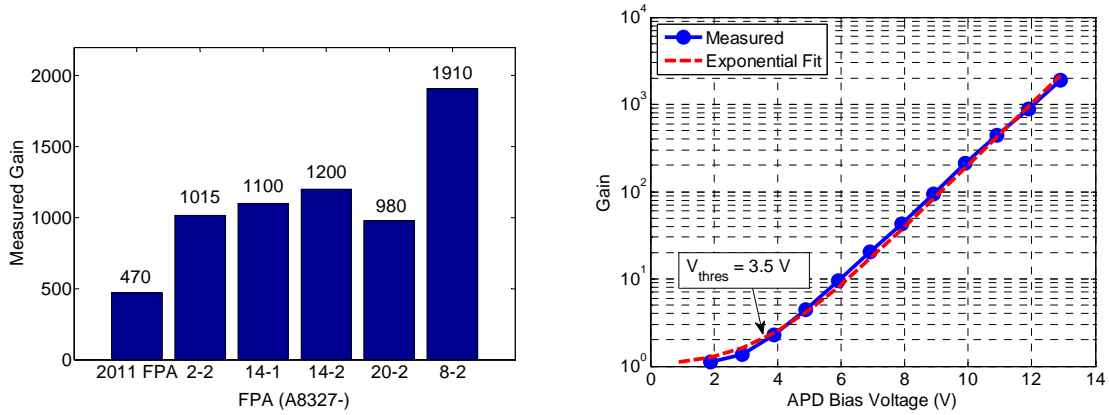


Figure 10: Left: Measured gain vs. array. Right: Measured and fit gain vs. voltage curves on Pixel 1,1 of A8327-8-2.

ii. Jitter

Jitter was measured using the pulsed laser focused in the middle of the four junctions. The leading edge of an external InGaAs photodiode was used as the time reference, and the time delay from when the leading edge of the analog output crossed a user-set threshold of 6 mV was measured using a LeCroy oscilloscope. 5000 pulses were accumulated for each jitter measurement. A8327-14-1's rms jitter was 1570 ps and A8327-8-2's was 2370 ps. On the 2011 array, the rms jitter was 632 ps. The increase in jitter in the current devices is due to the smaller junction diameters as the electron has a longer distance to diffuse leading to a longer time delay and rms jitter. The rms jitter can be decreased by placing the diodes on a closer pitch, and this will be implemented on future designs. 3D Monte Carlo random-walk electron diffusion modeling yields good agreement with measured data, and the results are summarized in Table 5 and Fig. 11.

Table 5: Summary of the modeled and measured jitter and eCE.

	A8327-8-2	A8327-14-1	2011 Array
Electron Mobility (model input)	29,000 (cm ² / (V·s))	26,000 (cm ² / (V·s))	26,000 (cm ² / (V·s))
Diffusion Length (model input)	20 μm	13 μm	13 μm
Junction Diameter (model input)	21 μm	25 μm	31 μm
Simulated rms jitter	2.38 ns	1.50 ns	0.764 ns
Measured rms jitter	2.37 ns	1.57 ns	0.632 ns

Simulated eCE	83%	79%	91%
Calculated eCE (Measured PDE_{max} * 1.08 for AR coating efficiency)	77%	71%	54%

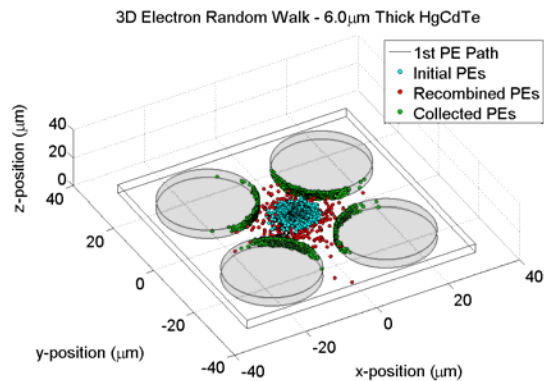


Figure 11: 3D Monte Carlo random-walk simulation results. The simulation performs diffusion of electrons in the p-type region and records how many photo-electrons (PEs) get collected, how many are lost to recombination, and also measures the time of arrival statistics to determine the jitter.

iii. Conversion Efficiency

As stated above, the net quantum efficiency (otherwise known as photon conversion efficiency, CE) of the pixel is the product of QE in the pixel active area (which depends on wavelength, AR coating, and the HgCdTe thickness), the eCE, and the fill factor. In our case where we are using a focused spot in the p-region, the fill factor is 100%. For 6 μm thick HgCdTe detector, at 1550 nm the device's QE is 90% to 99% depending on the AR coating. Modeling suggests the eCE is on the order of 80-90%, yielding a maximum PDE of 70-90% depending on diode geometry. Experimental data agrees, although typically the maximum PDE is on the low end of the range suggesting that the electron diffusion length might be slightly shorter than modeled.

iv. Excess Noise Factor

The excess noise factor was determined using three methods: fitting the event rate versus threshold voltage data measured with cw flux as shown in Section V, fitting pulse photon amplitude distribution data, or using the equation

below with 1 ns pulses of increasing photon numbers where n is the number of photons per pulse, μ is the mean of the output pulse amplitudes, and σ is the standard deviation of the output pulse amplitudes.

$$F = \left(\frac{\sqrt{n}}{\frac{\mu}{\sigma}} \right)^2$$

Each method verified the single photon excess noise factor is 1.2-1.3. The pulsed PDE was measured on A8327-14-1 with an average of 1 photon/pulse, and good agreement was found in fitting the data using an excess noise factor of 1.25 as shown in Fig. 12.

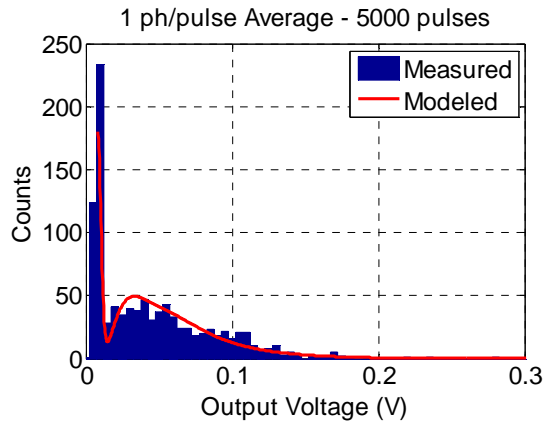


Figure 12: Histogram of 5000 pulse amplitudes with a 1 photon/pulse input signal. The modeled curve is a noise factor of 1.25.

d. Signal to Noise Ratio

The measured SNRs are shown in Table 6. The mean single photon voltages and rms noise voltages reported both include the external electronics' gain of +5 V/V. The rms noise was uniform across all 16 pixels at 3 mV on both of the current arrays, and is higher than the 2011 array due to optimization of ROIC biases for low FER. Although the noise increased, there was no effect on maximum PDE which enabled the low FER operation while maintaining good PDE.

Table 6: Summary of the mean single photon SNR.

Array	Bias	APD Gain	Mean Single Photon Voltage	RMS Noise	Mean Single Photon SNR
2011 Array	13 V	470	23.8 mV	2.0 mV	11.9
2011 Array	14 V	Not Measured	27.4 mV	2.0 mV	13.7
A8327-14-1	12.9 V	1100	37 mV	3.0 mV	12.3
A8327-8-2	12.9 V	1910	68 mV	3.1 mV	21.9

e. MTBE and Pulse Width

Using a ROIC gain of 125 kΩ, the minimum time between pulses was shown to be 9 ns, c.f. Fig. 13. Typical output pulses had a time to peak (TTP) of 5 ns with a 10-90% rise time of about 3 ns. This is similar to the previously reported results on the 2011 array. The Silvaco® Hipex parasitic extraction revealed that a significant amount of parasitic capacitance was present in the fabricated ROIC that wasn't accounted for in the design, limiting the electrical bandwidth and hence the TTP. Future designs of the ROIC will take the parasitic extraction analysis into account allowing the full designed bandwidth to be achieved.

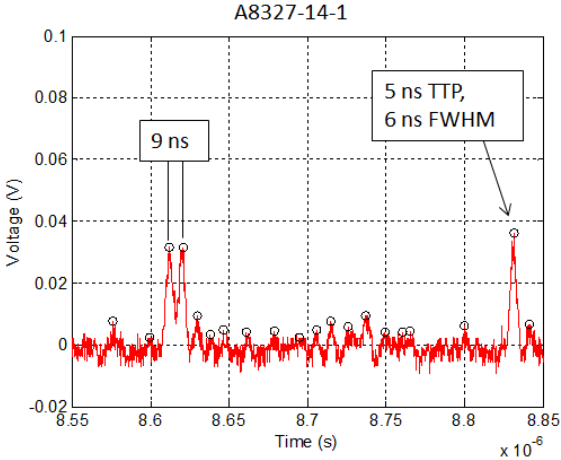


Figure 13: Analog output with peaks detected. Pulses closer than 10 ns together are easily discernable.

f. Operability

One pixel out of all pixels on five of the arrays that were tested had high dark current resulting in an operability of 98.75% across the arrays.

V. PDE vs. FER Model

A model was generated which explains the PDE vs. FER curve, including the downwards trend after the peak PDE is reached. Excellent fits to measured data were obtained, as shown in Fig. 14. The model generates an output voltage distribution for when the laser is on and for when the laser is off and then processes them exactly as the raw data is processed. Each distribution is comprised of a Gamma distribution for the excess noise factor of the APD added to a Gaussian distribution for the ROIC noise. The model provides a method to fit the excess noise factor of the APD with tight granularity as shown in Fig. 15. The downward trend after the peak PDE is due to a difference in the mean of the Gaussian ROIC noise when the laser is on versus when the laser is off. This is due to undershoot present in the tail of the impulse response of the ROIC. As more photons are incident upon the array, the mean of the noise shifts slightly causing the curve to bend down. Of course this isn't an issue during operation because the threshold will never be set in the ROIC's noise floor and the operating point will be on the left side of the curve.

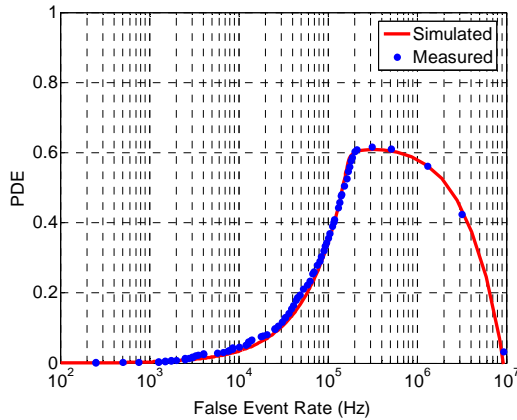


Figure 14: Modeled and measured PDE vs. FER data on A8327-14-1 pixel 1,1.

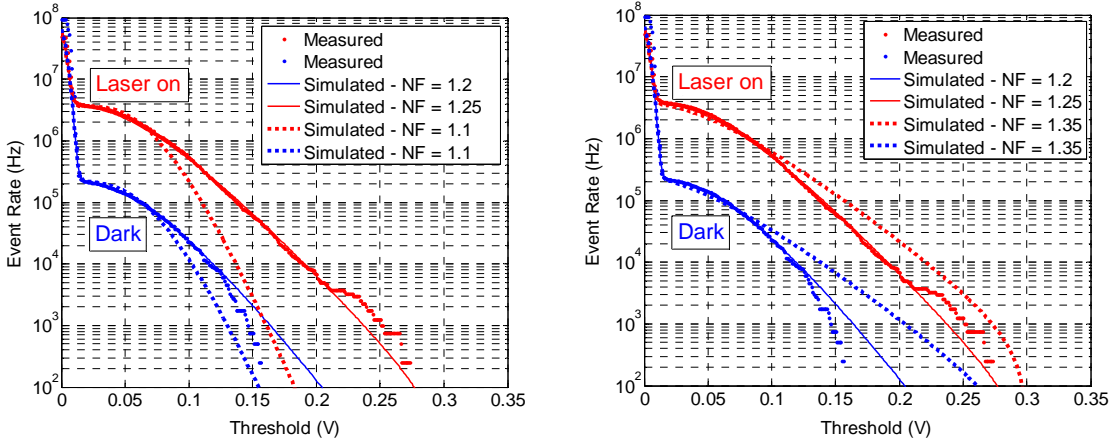


Figure 15: Left: Best fit to a noise factor of 1.2-1.25 (solid line), with an excess noise factor of 1.1 also shown. Right: Same fit compared to an excess noise factor of 1.35.

VI. Conclusions

The 2011 LMPC 2x8 arrays with photon counting sensitivity were successfully replicated with enhanced performance. It was experimentally verified that ROIC glow emitted photons artificially inflated the FER of the 2011 array, and the application of a single layer metal blocking layer and optimization of the ROIC biases reduced the FER by an order of magnitude to 100-200 kHz. Photon detection efficiencies of greater than 50% were routinely demonstrated across 5 arrays, with one array reaching 70%. High resolution pixel-surface spot scans were performed and the junction diameters of the diodes were measured. The junction diameter was decreased from 31 μm to 22 μm resulting in a 4x increase in APD gain from 470 on the 2011 array to 1910 on A8327-8-2. A 3D Monte Carlo random walk model was generated that showed good agreement with the measured junction diameters, rms jitter, and eCE. Mean single photon SNR's of over 20 were demonstrated at excess noise factors of 1.2-1.3. A PDE vs. FER model was also generated with good agreement to measured data.

References

- [1] J. D. Beck, R. Scritchfield, P. Mitra, W. Sullivan III, A. D. Gleckler, R. Strittmatter, R. J. Martin, *Proc. SPIE* 8033, 80330N (2011).
- [2] J. D. Beck, R. Scritchfield, P. Mitra, W. W. Sullivan III, A. D. Gleckler, R. Strittmatter, R. J. Martin, *Opt. Eng.* 53(8), 081905 (2014).

[3] M. Lanzoni, E. Sangiorgi, C. Fiegna, M. Manfredi, & B. Ricco, *IEEE Electron Device Letters*, 12(6), 341-343 (1991).

[4] J. D. Beck, M. Kinch, X. Sun, *Opt. Eng.* 53(8), 081906, (2014).

[5] J. Rothman, L. Mollard, S. Gout, and J. Wlassow, *J. Electron. Mater.* 40, 1757–1768 (2011).